INSTITUTE OF PHYSICS PUBLISHING and INTERNATIONAL ATOMIC ENERGY AGENCY NUCLEAR FUSION

Nucl. Fusion **43** (2003) 16–24 PII: S0029-5515(03)56251-2

Implosion and ignition of magnetized cylindrical targets driven by heavy-ion beams

A.J. Kemp[a], **M.M. Basko**[b] **and J. Meyer-ter-Vehn**

Max-Planck-Institut für Quantenoptik, Hans-Kopfermann-Str. 1, 85748 Garching, Germany

Received 30 July 2002, accepted for publication 13 November 2002
Published 12 December 2002
Online at stacks.iop.org/NF/43/16

Abstract

Implosions of cylindrical targets, directly driven by heavy-ion beams irradiated along the cylinder axis, are investigated by one-dimensional magneto-hydrodynamic simulations. In order to reduce heat losses from the hot fuel, which is enclosed by a metallic tamper, an axial magnetic field is introduced in the targets prior to implosions. We find that diffusive loss of magnetic flux out of the fuel leads to an accumulation of fuel material next to the cold pusher, causing a major problem for the efficiency of magnetized implosions. Magnetized target fusion (MTF) is an important application of magnetized cylindrical implosions. Looking for an optimum reference configuration for MTF with heavy-ion beams, we find the ignition threshold of magnetized cylindrical fusion targets to be at a driver pulse energy of about 10 MJ per centimetre target length; this value is nearly independent of target size and driver power, while the fuel temperature is required to be larger than 50 eV prior to implosions. Finally, we compare our reference case of an igniting MTF target to a standard indirect-drive heavy-ion fusion target.

PACS numbers: 52.58Hm, 52.65Kj

1. Introduction

Magnetized target fusion (MTF) stands for inertial confinement fusion (ICF) with an additional magnetic field to suppress heat losses out of the fuel. It has been discussed mostly in the context of spherically symmetric implosions [1]. Our present work is devoted to cylindrical targets, shown schematically in figure 1. Their main advantage is that the magnetic field geometry in this configuration is consistent with that of the target, in contrast to [1] where the targets are spherical. In magnetized implosions, suppression of heat conduction losses during implosions may compensate for the inherently lower compression in cylindrical geometry as compared to the spherical ones [2]. As discussed in previous publications, the ignition criterion on the fuel ρR product of the fuel density ρ and the fuel radius R is strongly reduced if the magnetic field is strong enough to confine the trajectories of alpha particles from nuclear reactions [2, 3]. This relaxation of the ignition conditions is a distinct property of MTF.

The first part of this paper deals with 'self-sustained magnetized implosions' (SSMI), giving the principal conditions under which magnetized implosions can be successful. In order to prevent rapid loss of magnetic flux out of the target, it is necessary to provide certain minimum values of the initial fuel temperature and of the product $(UR)_0$ of implosion velocity and initial fuel radius [4]. Still, a significant fraction of fuel gas escapes from the region of strong magnetic field and is swept into a thin cold layer on the fuel periphery because of the strong axial magnetic field in the fuel, which inhibits radial burn propagation by means of heat conduction and alpha transport. This effect causes a major problem for magnetized ICF targets, since it reduces the amount of hot fuel that contributes to fuel burn. It is also difficult to ignite this layer radially because of the strong axial magnetic field in the fuel.

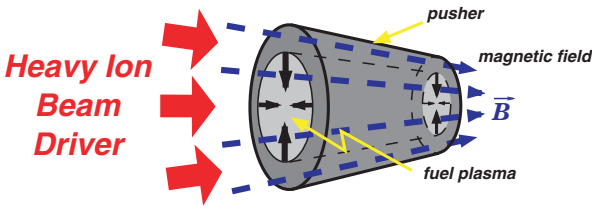

Figure 1. Magnetized cylindrical target, consisting of a metallic tube filled with thermonuclear fuel. An axial magnetic field ($\vec{B}$) is applied externally prior to implosions. The hollow driver ion beam heats an annular region of the metal tube, which expands radially and drives the inner part of the tube (pusher) towards the axis, as indicated by arrows. Typical target dimensions are envisaged as 1–3 mm in radius and 10–30 mm in length.

[a] Currently at: General Atomics, San Diego (CA), USA.

[b] On leave from: Institute for Theoretical and Experimental Physics, Moscow, Russian Federation.

Our main intention in this publication is to examine an igniting magnetized fusion target that operates at the lowest driver pulse energy possible. We present such a reference case, and discuss the dependence of the ignition threshold on key beam/target parameters. We also compare this reference target with the heavy-ion driven inertial fusion (HIDIF) design study for non-magnetized, spherical heavy-ion fusion (HIF) targets [5]. We find that magnetized implosions can achieve ignition conditions at significantly reduced values of implosion velocity, peak driver intensity, as well as relaxed conditions on driver pulse duration and convergence ratios of the implosions. A central conclusion of our work is that high-gain cylindrical fusion targets require hot-spot ignition, similar to spherical ICF. This means that a thermonuclear burn wave has to propagate along the axis, starting from an ignition sector, and ignite cold fuel in order to increase the overall target efficiency. The feasibility of burn-wave propagation in cylindrical DT columns has been demonstrated by means of two-dimensional computer simulations by Avrorin *et al* [6]. Our present work, however, is based on one-dimensional simulations which cannot treat the axial burn wave. Nevertheless our simulations are sufficient to describe the dynamics of hot-spot formation. Our study is therefore restricted to ignition conditions, where the hot spot is viewed as an axially uniform sector of an extended cylindrical configuration. The cylindrical implosions considered here are relatively slow; it is a major problem to reach ignition temperatures, due to the absence of strong shock heating in combination with the inefficiency of cylindrical convergence [2]. As a consequence, one has to start from high initial fuel temperatures (50 eV or more), which could be brought into the fuel from outside the target, e.g. by an axially incident laser pulse. This is essentially the scheme of injected entropy, as suggested recently by Caruso *et al* [7].

The numerical results presented here have been obtained by means of the one-dimensional magneto-hydrodynamics (MHD) code DEIRA, which includes diffusion equations for charged fusion products and nuclear burn equations for the relative abundances of the thermonuclear fuel among other features [4].

2. Efficient cylindrical implosions

The main objective of the cylindrical implosions discussed in this paper is to concentrate energy in a small amount of fuel mass in order to reach states of high energy density in matter. One way to drive such implosions is to irradiate targets with intense heavy-ion beams directly along the cylinder axis, as schematically indicated in figure 1. Before we describe the target set-up in more detail, we briefly discuss the deposition of heavy-ion beam energy in the target.

When an intense beam of heavy-ions impinges on matter, the kinetic energy of the ions is converted into heat. The resulting specific heating power P_i can be calculated from the stopping power $\mathrm{d}E_\mathrm{p}/\mathrm{d}\hat{R}$ via

$$P_\mathrm{i} = j_\mathrm{b}\frac{\mathrm{d}E_\mathrm{p}}{\mathrm{d}\hat{R}}, \qquad (1)$$

where $\mathrm{d}\hat{R} = \rho\,\mathrm{d}l$ is the so-called range increment, E_p is the ion particle energy, and j_b is the beam particle current density. Stopping powers and total ion ranges $\langle\rho l\rangle$ in matter depend in a non-trivial manner on the properties of the target material and the projectile [8]. Numerical simulations with realistic stopping power models show that the ion beam heating at an appropriate choice of beam particles/energies will be uniform along the cylinder axis up to 10% along the first 50–60% of the total ion range in the target, corresponding to a length of about 1–1.5 cm (for $_{131}\mathrm{Xe}^{+54}$ ions at $E_\mathrm{p} = 1.1$ GeV u^{-1} in solid gold [4]). Beyond this region, heating becomes extremely non-uniform. This fact could either be exploited to the benefit of overall target performance in two-dimensional target designs, or compensated by means of variable pusher thickness or cone-like two-dimensional target designs for example. However, in order to obtain an almost uniform ion beam deposition, we assume 'sub-range' targets, where the target length is smaller than the ion range.

The targets we consider in our work consist of a metal tube filled with thermonuclear fuel, i.e. deuterium or a deuterium–tritium mixture, at low density. The heavy-ion beam energy is assumed to be deposited in a radially bounded 'deposition layer' of the metal tube where it is converted into heat energy and causes an acceleration of the inner cold 'pusher' layer. Our initial target set-up is then defined by

$$\frac{R_\mathrm{f}}{R_\mathrm{b}} = 0.55, \qquad \frac{R_\mathrm{p}}{R_\mathrm{b}} = 0.6, \qquad \frac{R_\mathrm{tot}}{R_\mathrm{b}} = 1.5, \qquad (2)$$

where R_f is the radial position of the fuel/pusher interface, R_p the outer pusher boundary, and R_tot the total target radius before the implosion starts. All quantities are normalized to the outer beam radius R_b. These proportions correspond to an initial pusher aspect ratio $A_\mathrm{r} \equiv R_\mathrm{p}/(R_\mathrm{p} - R_\mathrm{f}) = 12$, which has been chosen for two reasons: first, the ratio of the cold pusher mass m_p to the deposition layer mass m_h is hereby fixed at a value of about 0.1, close to the optimum payload-to-shell mass ratio of an ideal rocket [9]. This yields an optimum conversion efficiency between the kinetic energies of exhaust gas and payload, or an optimum implosion efficiency in our case [4]. The second reason for our choice of the pusher aspect ratio is hydrodynamic stability of the imploding pusher. In order to prevent the pusher from breaking up during the implosion, it should not be too thin [9]. An immediate consequence of the fixed target proportions is that the radial layer structure of each target can be characterized by a single number, namely by the spot radius R_b of the ion beam. Note that expansion of the target material in axial direction is not accounted for in the present one-dimensional simulations. However, it should not be a problem for sufficiently long target cylinders. This issue has to be studied in more detailed investigations in the future, using two-dimensional MHD simulations.

3. Magnetized implosions

Before discussing the evolution of the boundary layer in magnetized implosions, we will briefly introduce the physics of SSMI that have been described in more detail in [4]. We will then address a similarity between magnetized implosions in which the SSMI key parameter is left invariant.

Assume that a uniform magnetic field B_0 parallel to the cylinder axis has been introduced in the target prior to an implosion. Due to the finite electrical conductivity of the

target material, magnetic flux will diffuse out radially, and competition of magnetic diffusion with implosion will be characterized by the magnetic Reynolds number Rm. The latter is defined as the ratio of magnetic diffusion time t_{md} to implosion timescale t_{i}

$$Rm \equiv \frac{t_{\mathrm{md}}}{t_{\mathrm{i}}} = \frac{U t_{\mathrm{md}}}{R} = \frac{4\pi\sigma}{c^2} U R, \tag{3}$$

where $\sigma_\perp$ denotes electrical conductivity, U implosion velocity and R target radius. Note that both pusher and fuel electrical conductivities are relevant for the magnetic field diffusion. On the other hand, competition between radial heat conduction losses and implosion is characterized by the Peclét number Pe, defined as the ratio of heat diffusion time t_{hc} to implosion timescale t_{i}

$$Pe \equiv \frac{t_{\mathrm{hc}}}{t_{\mathrm{i}}} = \frac{n_{\mathrm{e}} U R}{\kappa}, \tag{4}$$

where n_{e} is the electron number density and κ is the radial electron heat conduction coefficient (ion heat conduction is neglected in these rough estimates, but not in the MHD simulations). The impact of the magnetic field on the electron heat transport coefficient is characterized by the magnetization parameter $x_{\mathrm{e}} \equiv \omega_{\mathrm{e}}\tau_{\mathrm{e}}$, where $\omega_{\mathrm{e}} = eB/m_{\mathrm{e}}c$ is the electron gyrofrequency and τ_{e} is the electron–ion collision time [10]. Substituting Braginskii's expression for the heat conduction coefficient (see [4] for details), one obtains

$$Pe \propto U R \frac{\rho}{T^{5/2}} \frac{3.77 + 14.79 x_{\mathrm{e}}^2 + x_{\mathrm{e}}^4}{11.92 + 4.66 x_{\mathrm{e}}^2}. \tag{5}$$

In a magnetized plasma, where $x_{\mathrm{e}} \gg 1$, the electron heat conduction is suppressed by a factor of approximately x_{e}^{-2}, and the Peclét number increases correspondingly. As a consequence, heat insulation will improve as $Pe \propto C_{\mathrm{r}}^{5/3}$ during implosions. A detailed analysis reveals that the loss of magnetic flux from a cylindrically imploding volume can be characterized by two parameters defining the so-called SSMI regime [4]. The initial fuel temperature, T_0, and the initial value of the product of cylinder radius and implosion velocity $(UR)_0$, determine whether the magnetic flux will be nearly frozen-in and heat insulation improves during implosion, or if the magnetic flux will diffuse out and heat insulation decreases. For an initial value of the magnetic field $B_0 = 10\,\mathrm{T}$, the regime of SSMI can be roughly characterized by

$$\begin{aligned} T_0 &\geqslant 20\,\mathrm{eV}, \\ (UR)_0 &\geqslant 2 \times 10^4\,\mathrm{cm^2\,s^{-1}}. \end{aligned} \tag{6}$$

These limits depend only weakly on the exact value of B_0. The initial fuel density has to be optimized in each case to reduce bremsstrahlung energy losses [4].

3.1. Boundary layer

The diffusive loss of magnetic flux out of imploding cylindrical targets—which is unavoidable in realistic targets—shows up in the formation of a 'boundary layer', namely a region of strongly increasing fuel density next to the fuel-pusher interface, which grows in mass as the implosion proceeds [4]. As an example, figure 2 shows radial profiles of density, ion temperature, the magnetic field and fluid velocity in an imploding cylinder at a time when the radial convergence ratio is $C_{\mathrm{r}} = 20$ (for the target parameters, see table 1). In the figure, one can clearly see the boundary layer of cold, dense plasma at the fuel-pusher interface with strong radial gradients of the given quantities. For clarity, the layer is marked by a vertical shaded band.

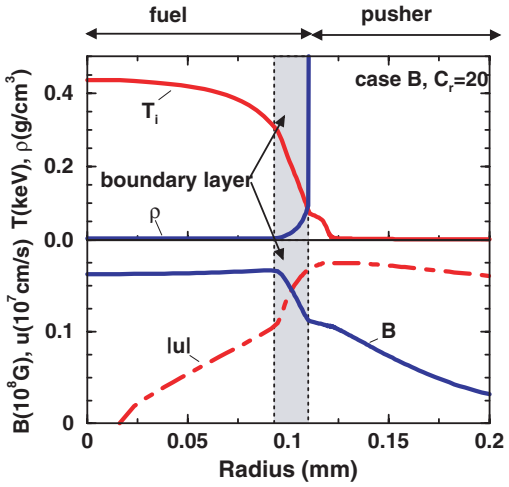

Figure 2. Radial profiles of density ρ, ion temperature T_{i}, magnetic field B, and the (negative) flow velocity U in the inner part of target B (cf table 1), at time $t = 260\,\mathrm{ns}$, corresponding to $C_{\mathrm{r}} = 20$. The region of strong density and magnetic field gradients is called boundary layer (marked by a grey band). Domains of fuel and pusher material are marked by arrows on top of the figure.

The importance of the boundary layer lies in its negative effect on our aim to reach states of hot, dense plasma in magnetized cylindrical implosions. As can be seen in figure 2, the fuel in the boundary layer is cold compared to the central region and has a weaker magnetic field—i.e. has a significantly lower than in the centre value of the magnetization parameter x_{e}; as a result, heat exchange with the metal liner keeps the temperature of this layer relatively low. For magnetized fusion targets, this means that a large part of fuel will be difficult to ignite, compare section 4.

In order to get a quantitative understanding of the growth rate of the boundary layer during implosions, figure 3 compares the evolution of boundary layers in several magnetized implosions. As a definition, the inner edge of the boundary layer is taken at a radius where the fuel density is twice its overall minimum value. Figure 3 plots the ratio $x_{\mathrm{m}} = M_{\mathrm{bl}}/M_{\mathrm{f}}$ of the amount of fuel mass in the boundary layer M_{bl} to the total fuel mass M_{f} versus the time-dependent radial convergence ratio $C_{\mathrm{r}}(t) = R_{\mathrm{f}}(0)/R_{\mathrm{f}}(t)$. Results are shown for targets A and B (for parameters, cf table 1), and an additional case C with $R_{\mathrm{b}} = 20\,\mathrm{mm}$; parameters of the latter case are equal to those of target B, except that initial radius and pulse duration t_{p} are scaled according to equation (9). The main results from figure 3 can be given in the following two statements: (i) to a good accuracy, the amount of fuel $x_{\mathrm{m}}(t)$ in the boundary layer evolves with the convergence ratio $C_{\mathrm{r}}(t)$ of an implosion as

$$x_{\mathrm{m}}(t) = g_{\mathrm{c}} \ln C_{\mathrm{r}}(t) + x_{\mathrm{m0}}, \tag{7}$$

where g_{c} and x_{m0} depend on the implosion parameters. An important result of the numerical simulations is that the value of

Table 1. Parameters of magnetized implosions A and B. Given are the focal spot radius R_b of the ion beam, initial fuel density ρ_0, initial magnetic field B_0, and the value of the $(UR)_0$ product. Corresponding target proportions can be derived from R_b and equation (2). Both implosions are driven by an ion beam with $P_i = 1\,\mathrm{TW\,g^{-1}}$, the initial fuel temperature is $T_0 = 20\,\mathrm{eV}$. Also given are the implosion results, i.e. peak temperature T_m and expected neutron yield N_n from D_2 thermonuclear reactions. Results of corresponding non-magnetized implosions are given as well.

	R_b (mm)	ρ_0 ($\mathrm{g\,cm^{-3}}$)	B_0 (T)	$(UR)_0$ ($\mathrm{cm^2\,s^{-1}}$)	T_m (keV)	N_n ($\mathrm{cm^{-1}}$)	$T_m(B=0)$ (keV)	$N_n(B=0)$ ($\mathrm{cm^{-1}}$)
A	0.8	1×10^{-4}	30	2.4×10^4	0.3	10^4	0.2	10^3
B	4.0	3×10^{-5}	10	1.7×10^5	1.1	10^9	0.4	2×10^6

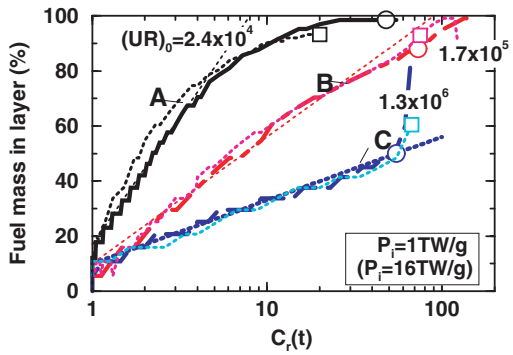

Figure 3. Evolution of the boundary layer mass in several magnetized implosions, i.e. ratio of fuel mass in the boundary layer to total fuel mass, versus radial convergence $C_r(t) \equiv R_f(0)/R_f(t)$ (bold lines). Parameters of cases A and B are described in table 1. An additional case C is characterized by $R_b = 20\,\mathrm{mm}$, and fuel parameters equal to those of target B. Also given is the $(UR)_0$ parameter of each implosion in units of $\mathrm{cm^2\,s^{-1}}$ next to the graphs. Peak compression is marked by circles. Thin straight lines indicate scaling relations $x_m = g_c \ln C_r(t) + x_{m0}$ for the mass accumulation in the layer. Additionally, results are shown for a second set A*, B*, C* of magnetized implosions explained in section 3.2. Peak fuel compression in the second set is marked by boxes.

g_c depends essentially on the $(UR)_0$ product, and only weakly on the initial fuel density ρ_0 and temperature T_0. This holds as long as the SSMI initial conditions (6) are satisfied [4]. (ii) The slope g_c in equation (7) scales with $(UR)_0$ as

$$g_c \propto (UR)_0^{-0.35}. \tag{8}$$

A comparison of the cold fuel mass accumulated in the boundary layer in cases A and B (see figure 3) reveals the origin of the smaller neutron yield from implosion A as compared to implosion B as given in table 1. While the boundary layer in implosion A contains more than 95% of the fuel mass at peak compression, it is only half of this value in implosion B.

Qualitatively, the formation of the boundary layer can be explained as follows. Due to the cooling of the fuel next to the pusher, its electrical conductivity decreases. This causes an increased loss of magnetic flux, which further decreases the fuel magnetization and increases the cooling rate of the boundary layer with respect to the hot central fuel. Note that the development of the cold boundary layer resembles the development of the thermal instability [11].

3.2. Similarity between magnetized implosions

In order to reduce the available parameter space, we now demonstrate an important scaling property of magnetized implosions. Figure 3 includes results for an additional set of three implosions (A*, B*, C*). This second set of target is scaled such that the $(UR)_0$ product remains the same as in the corresponding case of the first set. The initial conditions (ρ_0, T_0, B_0) in each implosion of the second set are identical to those of the first set. As will be shown below, this procedure is equivalent to keeping the product $P_i R_b^4$ of the specific deposition power P_i of the ion beam and the beam radius R_b constant. In figure 3, the second set of implosions has been obtained by applying the rule

$$R_b(\mathrm{A}^*) = 2R_b(\mathrm{A}), \qquad P_i(\mathrm{A}^*) = \tfrac{1}{16} P_i(\mathrm{A}),$$

similar for the cases B* and C*. One can see in figure 3 that the evolution of the boundary layer in the scaled targets follows closely the one in their original counterparts, so that one can indeed speak of a similarity.

Let us now express the key 'implosion parameter' $(UR)_0$ in terms of the 'beam' parameter $P_i R_b^4$, assuming equal radial proportions for all targets as given in equation (2) above. By this assumption, the deposition layer dimensions $R_p < r < R_b$ are fixed by the choice of R_b. We are further assuming that the total pulse duration t_p of the ion beam is consistent with the effective irradiation time

$$t_H \simeq \frac{R_b^{2/3}}{P_i^{1/3}}, \tag{9}$$

which is the approximate travel time of a rarefaction front in a plane solid target heated by an ion beam, for the distance R_b [12]. Using a constant hydro conversion efficiency η_H from thermal energy by beam heating into kinetic implosion energy (see [4] and references therein), one arrives at the expression $U^2/2 = \eta_H P_i t_H$ for the implosion velocity, or at

$$(UR)_0 \simeq \sqrt{2\eta_H \left(\frac{R_0}{R_b}\right)^2} (P_i R_b^4)^{1/3}. \tag{10}$$

This means that the $(UR)_0$ product is directly related to the 'beam' parameter $P_i R_b^4$. The $(UR)_0$ product is also a measure of the total driver energy E_b deposited in the target, as can be seen from combining equation (10) and

$$E_b = A t_H P_i R_b^2 \equiv A (P_i R_b^4)^{2/3}, \tag{11}$$

where $A = \pi(1 - R_f^2/R_b^2)\rho_{0p}$ and ρ_{0p} is the pusher material density. Accounting for all pre-factors and using the lower bound for $(UR)_0$ for the SSMI regime given in equation (6), this gives a estimate for the lower bound on the driver pulse energy that is required for a magnetized implosion

$$E_{b\min} \gtrsim 20\text{–}40\,\mathrm{kJ\,cm^{-1}}, \tag{12}$$

depending only weakly on the exact fuel parameters. At a specific driver power of $P_\mathrm{i} = 1\,\mathrm{TW\,g^{-1}}$, this corresponds to a lower limit on the ion beam focal-spot radius of $R_{\mathrm{b}\min} \gtrsim 1.4\,\mathrm{mm}$, as can be easily checked in equation (10). This limit is also in reasonable agreement with the simulations presented above.

4. Magnetized fusion targets

Applying the results of the previous section to magnetized fusion targets, our aim is now to find an igniting target at the lowest driver pulse energy possible. First, we will present such a reference case and determine its ignition threshold with respect to the key parameters: specific driver power, initial fuel density, temperature and magnetic field strength. Second, we will discuss the ignition and burn stage of magnetized fusion targets in more detail, including a comparison of the reference case with results of the HIDIF design study [5]. Third, we will discuss scaling properties of magnetized fusion targets with the radial target size. The relative target proportions assumed in this section are identical to those described above (see equation (2)). However, the specific heating power and initial fuel temperatures in the fusion targets have to be significantly higher than the values used earlier. The fuel is now assumed to be a deuterium–tritium mixture.

4.1. Ignition threshold

Once a focal spot radius of the ion beam has been chosen the target geometry is determined, and the remaining free parameters are the initial fuel density ρ_0, the initial fuel temperature T_0, the initial magnetic field B_0, and the specific driver power P_i. We first determine these parameters on the basis of a simple estimate, and check them by computer simulations afterwards.

The heated mass per unit length in a consistent target set-up is $M_h \simeq \pi(R_\mathrm{b}^2 - R_\mathrm{p}^2)\rho_\mathrm{h}$. Using equation (9) for the consistent heating time t_H, the specific driver power P_i is related to the beam energy via $E_\mathrm{b} \simeq t_\mathrm{H} P_\mathrm{i} M_\mathrm{h}$. Assuming $1\,\mathrm{mg\,cm^{-1}}$ of DT fuel in the target, one needs about $20\,\mathrm{MJ\,cm^{-1}}$ of driver energy for ignition. As a consequence, the specific driver power P_i is

$$P_\mathrm{i} \simeq E_\mathrm{b}\, t_\mathrm{H}^{-1}\, M_h^{-1} \propto E_\mathrm{b}^{3/2}\, R_\mathrm{b}^{-4} \approx 100\text{–}200\,\mathrm{TW\,g^{-1}}. \quad (13)$$

At the low implosion velocities corresponding to such driver parameters, i.e. $U \lesssim 10^7\mathrm{cm\,s^{-1}}$, we expect no strong shock heating occurs during implosions [13]. Therefore, the fuel heating in magnetized implosions can be described in the approximation of a quasi-adiabatic compression, in the best case. (In general, finite losses cannot be avoided). This approximation assumes that fuel density ρ, temperature T and the magnetic field B scale with the radial convergence ratio $C_\mathrm{r}(t) \equiv R_\mathrm{f}(0)/R_\mathrm{f}(t)$ as [4]

$$\rho \propto C_\mathrm{r}^2, \qquad T \propto C_\mathrm{r}^{4/3}, \qquad B \propto C_\mathrm{r}^2. \quad (14)$$

To reach thermonuclear ignition temperatures of 5–10 keV in such implosions, the fuel needs to have $T_0 = 150\text{–}250\,\mathrm{eV}$ initially, assuming a moderate value of $C_\mathrm{r} = 15$ at peak compression. Additionally, to get the fuel magnetization

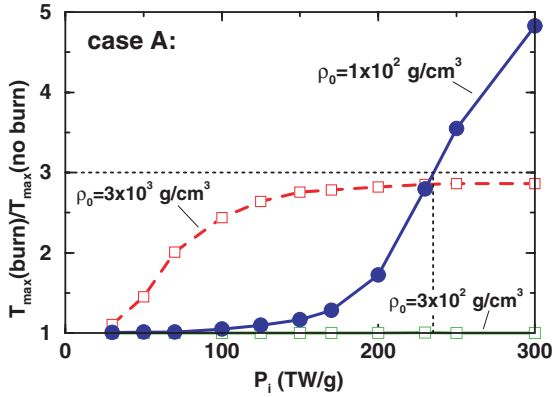

Figure 4. Ignition curves for case A (cf table 3). Plotted is the ratio of peak fuel temperature results with fusion reactions to results without fusion reactions versus specific driver power P_i. Three ignition curves for different values of the initial fuel density ρ_0 are shown, while the fuel initial conditions $T_0 = 300\,\mathrm{eV}$ and $B_0 = 50\,\mathrm{T}$ are kept fixed. Ignition has occurred if the ignition ratio defined above exceeds a factor of three. This limit is marked by a horizontal dotted line.

$BR \gtrsim 6 \times 10^5\,\mathrm{G\,cm}$ required for ignition [3], the initial magnetic field B_0 needs to be about $B_0 \gtrsim 10\text{–}50\,\mathrm{T}$.

As the second step, we determine the ignition threshold of magnetized implosions by means of one-dimensional MHD simulations for fixed initial fuel conditions $T_0 = 300\,\mathrm{eV}$ and $B_0 = 70\,\mathrm{T}$. With each combination of P_i and ρ_0, two simulations are carried out: one with fusion reactions, one without. In figure 4, the ratio of the resulting peak fuel temperatures is plotted versus driver power P_i for three values of the initial fuel density ρ_0. Only if the peak temperature ratio is greater than three, the fuel is called ignited. The resulting curves connecting implosions with equal values of ρ_0 are called 'ignition curves'. Figure 4 shows that the initial fuel density ρ_0 needs to be optimized for each parameter set (P_i, B_0, T_0). There exists an optimum value of ρ_0 because, on the one hand, the fuel mass determines the maximum thermonuclear energy yield of the target; so one would like ρ_0 to be as large as possible. On the other hand, if ρ_0 is too large, ignition will not occur as the implosion is stopped by the fuel pressure.

4.2. Ignition threshold dependence on initial parameters

In order to reach ignition conditions at the end of an implosion, one needs either large convergence ratios C_r, or high initial fuel temperatures T_0. Experimentally, both are difficult to reach: large C_r go along with hydrodynamic instabilities (which we do not analyse in this publication (see [4] for comments)), while high T_0 values are difficult to achieve technically. At present, we cannot answer the question for an optimum compromise. Nevertheless, in the following we systematically explore the corresponding parameter space by means of MHD computer simulations.

Our strategy is to fix a certain $(UR)_0$ value by keeping P_i and R_b constant, and to check various combinations of B_0 and T_0 in the range

$$30\,\mathrm{eV} \lesssim T_0 \lesssim 1000\,\mathrm{eV}, \quad (15)$$

$$5\,\mathrm{T} \lesssim B_0 \lesssim 200\,\mathrm{T}, \quad (16)$$

for ignition. For each point, we seek an optimum value for the initial fuel density where ignition still occurs. To find this optimum we have varied ρ_0 in the range

$$1 \times 10^{-4}\,\mathrm{g\,cm^{-3}} \lesssim \rho_0 \lesssim 1 \times 10^{-2}\,\mathrm{g\,cm^{-3}} \qquad (17)$$

and marked the case by a symbol in a (T_0, B_0) plane. Note that it is important for the completeness of our survey that none of our igniting cases is at the borders of interval (17). In figure 5, full symbols represent ignition, while empty symbols correspond to the cases where ignition has not occurred. For all implosions presented in figure 5, the ion beam radius is kept constant at $R_\mathrm{b} = 3.0\,\mathrm{mm}$, and the ion pulse is assumed to heat the target shell with constant deposition power $P_\mathrm{i} = 230\,\mathrm{TW\,g^{-1}}$ up to the moment of stagnation.

The first observation in figure 5 is that ignition occurs only in a narrow region of the (T_0, B_0) parameter space. The limits of this 'ignition island' are mainly set by the conditions for SSMI and by magnetic pressure. Initial configurations with $B_0 \lesssim 20\,\mathrm{T}$ or $T_0 \lesssim 20\,\mathrm{eV}$ will not meet the SSMI requirements, i.e. heat diffuses rapidly out of the fuel. For too large values of $B_0 > B_{0\max} \propto T^{0.75}$, on the other hand, ignition will not occur as the implosion is stopped by magnetic pressure. Note that the ignition island is also bounded towards large initial temperatures, for the following reason: as T_0 is increased, the fuel compression, and therefore also the maximum fuel ρR, decrease. As a consequence, the final yield and the peak fuel temperature drop slightly. At the same time, the peak fuel temperatures in the reference implosions (without burn) increase with growing T_0, causing the ignition ratio to drop below three.

Figure 5 also presents the maximum convergence ratios C_r for each igniting configuration, taken at the optimum fuel density $\rho_{0\mathrm{m}}$. The C_r values decrease from extremely large values, i.e. $C_\mathrm{r} = 100$, as found in implosions with $B_0 = 20\,\mathrm{T}$ and $T_0 = 30\,\mathrm{eV}$, down to $C_\mathrm{r} \simeq 16$ for $B_0 = 200\,\mathrm{T}$ and $T_0 = 300\,\mathrm{eV}$. In addition to the limits of the ignition island as seen in figure 5, the radial convergence ratios C_r provide a means to select acceptable implosion parameter combinations B_0 and T_0. In order to reduce the effect of Rayleigh–Taylor instabilities during an implosion, one might restrict to convergence ratios $C_\mathrm{r} \lesssim 20$ [4].

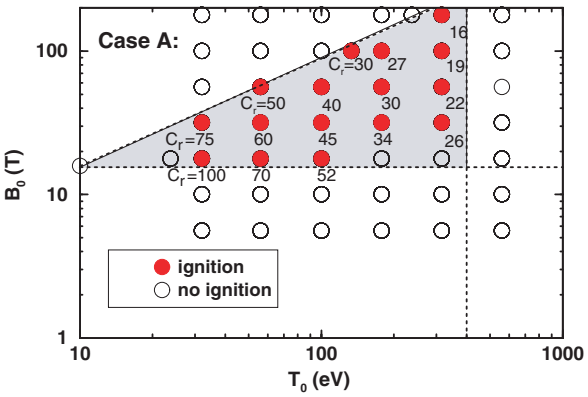

Figure 5. Igniting (●) and non-igniting (○) cases in the plane spanned by the initial fuel temperature T_0 and the magnetic field B_0 for fixed values of $R_\mathrm{b} = 3.0\,\mathrm{mm}$ and $P_\mathrm{i} = 230\,\mathrm{TW\,g^{-1}}$, and optimized values ρ_0. The maximum convergence ratios C_r of the implosions are given as numbers below the symbols.

It turns out that the largest initial fuel density $\rho_{0\mathrm{m}}$ for which ignition still occurs at given combinations of T_0, B_0, grows with the initial fuel temperature. At the same time, the convergence ratios C_r decrease, as seen in figure 5. This is connected with the ignition conditions for thermonuclear fusion, i.e. the minimum fuel temperature and ρR that have to be achieved at peak compression. Going from an igniting case to a larger initial temperature, the compression drops and so does the final ρR. To compensate for this, one has to go to larger initial fuel densities.

4.3. Ignition and burn

Let us now discuss the igniting reference implosion introduced above in more detail. Figure 6 shows the evolution of the average fuel temperature and magnetic field on the target axis of an igniting magnetized implosion. In addition, it presents the free-fall line for this implosion, which characterizes the time $t \simeq 45\,\mathrm{ns}$ when instabilities can reach the cylinder axis in the worst case. Notice that the fuel temperature is raised—due to the thermonuclear fusion reactions—by a factor of three in comparison to an implosion without burn (cf figure 4). As a consequence, the fuel temperature in the reference implosion is still growing when the free-fall line reaches the axis. This is not the case in the magnetized implosion A of the previous section; it should affect the stability of the pusher during the hot-spot formation in magnetized implosions and has to be discussed in future, two-dimensional studies of magnetized implosions.

Figure 7 shows radial profiles of temperature and density in implosion A at the time of peak compression, i.e. $t = 44.5\,\mathrm{ns}$, and at peak fuel temperature, $t = 46.5\,\mathrm{ns}$. Notice the gradients in fuel density, temperature and magnetic field, as discussed in section 3, which are characteristic for the magnetic boundary layer (cf figure 2). At ignition, about 40–50% of the fuel are contained in the boundary layer and therefore cannot contribute to burn since radial propagation of electrons and alpha particles is suppressed by the strong axial magnetic field. This is in strong contrast to the physics in spherical, non-magnetized ICF targets where radial burn propagation into cold fuel layers is desirable in order to reach high gain. Figure 7 also presents the radial dependence of the quantity B/ρ. In a quasi-adiabatic implosion with a fully

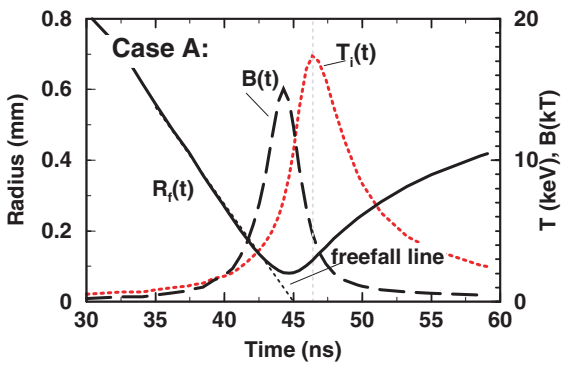

Figure 6. Evolution of fuel parameters in case A. Shown are the radial position of the fuel-pusher boundary $R_\mathrm{f}(t)$ (left scale), fuel ion temperature T_i, and the magnetic field B on the axis (right scale) versus time. Additionally, the free-fall line of the fuel-pusher interface is marked by a dotted line.

frozen-in magnetic field, this quantity would be uniform in space and time. Here, it remains constant throughout the main part of the fuel volume and drops only in the magnetic boundary layer. For a comparison between cylindrical MTF and a non-magnetized, *spherical* ICF capsule, we chose the HIDIF design study [5]. The latter is a result of a comprehensive study of indirectly driven, non-magnetized ICF capsules in spherical geometry. In general, the indirect-drive approach to ICF [9] assumes that small DT pellets are placed in metal cavities which are heated by external drivers. Capsule implosions are then driven by thermal x-rays from the hohlraum walls. Due to the stronger compression in spherical implosions, as compared to the cylindrical ones, the peak fuel densities in such capsules exceed those in cylindrical implosions significantly; therefore, burn is much faster. Additionally, hot-spot ignition with radial burn waves propagating into cold fuel brings the energy gain up to large values $G \simeq 100$ [5].

Table 2 compares our MTF reference case with results of the HIDIF study for an indirectly-driven fusion capsule in a hohlraum cavity that is heated by heavy-ion beams. The value for the specific driver power P_i in this case corresponds to a peak value and the pulse duration given here is the timescale of one sub-pulse (see figure 3 of [5]). The strong time-dependence of the ion pulses for indirect-drive targets makes great demands on the performance of accelerators. It is, however, necessary in order to obtain optimum implosion results in terms of the fuel density, temperature distributions required for hot-spot ignition. For the directly driven cylindrical targets discussed here, on the other hand, the beam pulses of the heavy ions are assumed to be uniform in space and time.

From the target physics point of view the distinct feature of the magnetized implosion lies in (i) the lower implosion velocity and (ii) lower fuel ρR at maximum compression. Regarding the implosion results in terms of gain G and burn fraction ϕ_b, one has to be aware of the fact that the magnetized target represents only an ignition section of a longer cylindrical target. High gain can be reached only with hot-spot ignition, as discussed above.

4.4. Ignition threshold dependence on target radius

Finally, we want to discuss the dependence of the ignition threshold of magnetized fusion targets on the target radius. We therefore present an alternative MTF target with beam radius $R_b = 5$ mm and accordingly scaled target dimensions (see table 3). To start, let us scale the driver power $P_i = 230\,\mathrm{TW\,g^{-1}}$ required for ignition in the reference case with $R_b = 3$ mm according to the procedure discussed above, compare equation (11). Since the driver pulse energy E_b is related to the specific driver power P_i and the focal spot radius R_b via $E_b \propto (P_i R_b^4)^{2/3}$, the driver power in the alternative target will be approximately

$$P_i(\mathrm{alt}) = \left(\tfrac{3}{5}\right)^4 P_i(\mathrm{ref}) \simeq 30\,\mathrm{TW\,g^{-1}}. \qquad (18)$$

Using similar initial fuel parameters T_0, B_0 to those chosen in the reference case, our simulations of the alternative target implosion show that (i) the ignition threshold is approximately $P_i \simeq 30\ \mathrm{TW\,g^{-1}}$, as predicted by equation (18), and (ii) the corresponding value of the initial fuel density ρ_0 is smaller in the alternative case compared to the reference case. The difference in the total beam energies E_b seen in table 3 shows that the scaling given in equation (11) becomes inaccurate, due to geometrical effects.

The dependence of ignition on the choice of initial parameters T_0 and B_0 is characterized in figure 8, giving the (T_0, B_0) parameter space region for which case B targets ignite. One can see that the ignition island for the case B is significantly smaller in the parametric (T_0, B_0) plane, and that the fuel density values for which ignition occurs are generally smaller than in the reference target.

The scaling that relates the two cases also has another important consequence: the $(UR)_0$ parameter is the same in both implosions, following from

$$(UR)_0 \propto (P_i R_b^4)^{1/3} \propto E_b^{1/2}, \qquad (19)$$

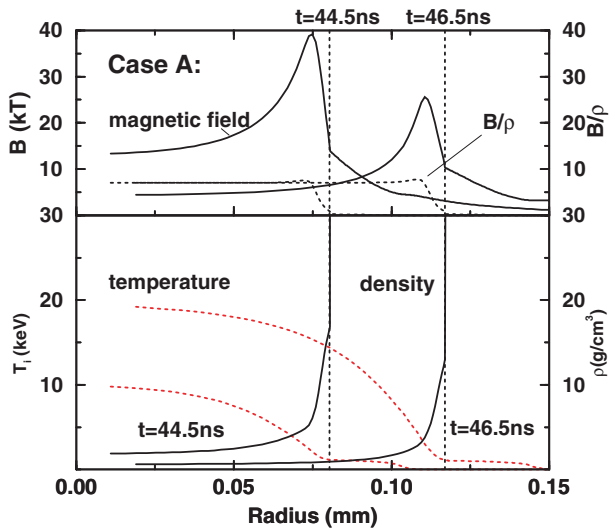

Figure 7. Profiles of ion temperature, density and magnetic field in implosion A for two times, corresponding to peak compression ($t = 44.5$ ns) and peak fuel temperature ($t = 46.5$ ns). The position of the fuel-pusher interface at these times is indicated by dotted vertical lines. Additionally, the ratio B/ρ (in $\mathrm{kT\,cm^3\,g^{-1}}$) is plotted in the upper diagram.

Table 2. Comparison of the magnetized cylindrical target A and HIDIF results [5]. Given are: pulse energy E_b, driver focal spot radius R_b, pulse duration t_p, peak specific driver power P_i, implosion velocity U (in $\mathrm{cm\,s^{-1}}$), initial magnetic field strength (in T), initial fuel temperature (in eV), peak fuel ρR value $(\rho R)_m$ (in $\mathrm{g\,cm^{-2}}$), maximum radial convergence ratio C_r, burn fraction ϕ_b and the gain G. Note that the gain of the reference target refers only to the ignition section discussed here.

	R_b (mm)	E_b	t_p (ns)	P_i(max) ($\mathrm{TW\,g^{-1}}$)	U ($\mathrm{cm\,s^{-1}}$)	B_0 (T)	T_0 (eV)	$(\rho R)_m$ ($\mathrm{g\,cm^{-2}}$)	C_r	ϕ_b (%)	G
HIDIF	3	5 MJ	10	10^4	3×10^7	—	—	2.75	30	35	90
MTF	3	$1\,\mathrm{MJ\,mm^{-1}}$	30	230	5×10^6	60	300	0.01	22	2.8	1

Table 3. Comparison of magnetized fusion targets A and B. Given are: ion pulse energy E_b, driver focal spot radius R_b, pulse duration t_p, peak specific driver power P_i, implosion velocity U (in cm s^{-1}), initial magnetic field strength (in T), initial fuel temperature (in eV), peak fuel ρR (in g cm^{-2}), peak fuel temperature T_m and burn fraction ϕ_b. Corresponding convergence ratios can be taken from figures 5 and 8.

	R_b (mm)	E_b (MJ mm^{-1})	t_p (ns)	P_i^{max} (TW g^{-1})	U (cm s^{-1})	B_0 (T)	T_0 (eV)	$(\rho R)_m$ (g cm^{-2})	T_m (keV)	ϕ_b (%)
Case A	3	1	30	230	5×10^6	60	300	0.01	18	2.8
Case B	5	1.8	75	30	3×10^6	60	300	0.012	19	2.5

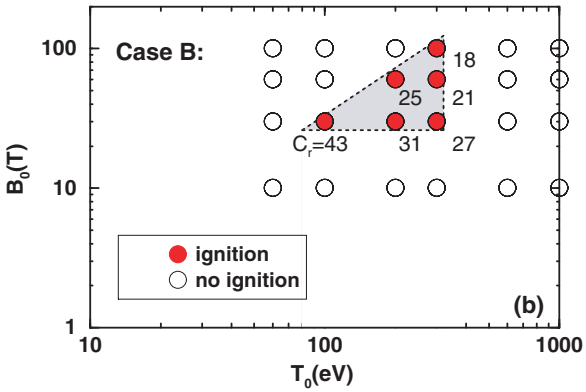

Figure 8. 'Ignition island' of the alternative case: igniting and non-igniting implosions in a plane of initial implosion parameters, cf the caption of figure 5.

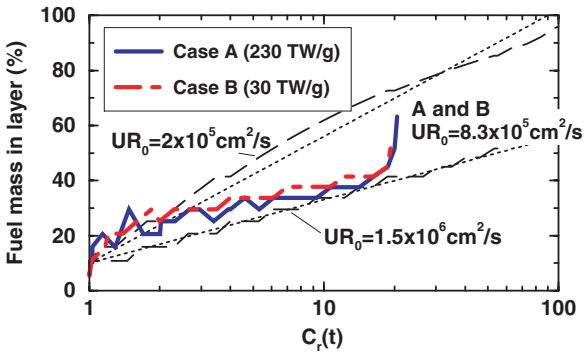

Figure 9. Evolution of the boundary layer in the magnetized fusion targets A and B, cf table 3. Plotted is the ratio of the fuel mass in the boundary layer to the total fuel mass versus radial convergence $C_r(t) \equiv R_f(0)/R_f(t)$. For comparison, two additional plots for the implosions B and C, from section 3, are included. The corresponding $(UR)_0$ values are given next to the plots.

compare equation (11). The value of the $(UR)_0$ product of the implosions discussed here is given in figure 9.

Figure 9 discusses the growth of the magnetic boundary layer in the respective implosions, presenting the fuel mass fraction in the cold boundary layer in both MTF implosions similar to figure 3 above. In order to compare their evolution with the SSMI presented above, the figure includes the magnetized targets A and B. Similar to these, the boundary layers of the targets evolve according to equation (7).

From the growth rate of the boundary layer in MTF targets A and B shown in figure 9, one can see that they are both well inside the SSMI regime of magnetized implosions. From figure 4, one can conclude that for lower $(UR)_0$, ignition is not possible. On the other hand, choosing implosions at larger $(UR)_0$ values does not significantly reduce the fraction of fuel lost to the cold boundary layer. One cannot expect a significant improvement of the target gain since most of the 'available' fuel inside the magnetic boundary layer is burnt.

In order to further relax the demands on heavy-ion drivers, one might attempt to design to design targets for fixed and reasonably low driver energies as given above, but for extremely large pulse durations and correspondingly low driver intensities—such targets would become very large, as equation (11) shows. However, our results show that the ignition island in the (B_0, T_0) parametric plane shrinks for decreasing driver intensity, and finally vanishes; this sets a lower limit for the possible driver intensity. In addition, the range of fuel densities ρ_0 for which ignition occurs shifts to smaller values with decreasing driver intensities P_i. As a consequence, the fusion energy yield would decrease, reducing the chances of getting the propagating thermonuclear burn wave that is required for high gain.

4.5. Losses along the cylinder axis

An important issue that is raised naturally when presenting one-dimensional studies of cylindrical heavy-ion beam targets is that of energy—and mass losses along the cylinder axis in the course of an implosion; these end-losses are not included in our simulations. However, we argue that they are negligible in the parameter regime relevant for this work, for the following reasons. In general, end-losses along the cylinder axis during an implosion include energy losses due to (i) radiation, (ii) electronic heat conduction, (iii) fast alpha particle losses, and mass losses caused by hydrodynamic motion. Consider the parameters of the MTF reference target presented in table 3 with an initial length-to-diameter aspect ratio of approximately 1–3. Assuming a radial convergence ratio $C_r \approx 20$, the aspect ratio grows to values >20–60 after the implosion. At a radial fuel $\rho R = 0.01$–0.03 g cm^{-2} at maximum compression, the corresponding value along the axis will be of the order $\rho z > 0.2$–2 g cm^{-2}. Comparing these numbers to the requirements for non-magnetized spherical ICF targets [9], we conclude that electronic heat conduction and alpha particle losses along the axis will be small enough not to quench ignition. Further, the maximum (fuel) mass loss along the axis caused by hydrodynamic motion can be estimated from the sound velocity $c_s \approx 4 \times 10^7\, T_{keV}^{1/2}$ cm s^{-1} in the fuel. Assuming an initial fuel temperature of 300 eV, as given in table 3, and using the implosion time given in figure 6, the minimum target length is several millimetres; this is consistent with the initial target size given above.

Finally, we want to stress that this work is not intended as specific two-dimensional MTF design study; instead, our aim is to explore the parameter-space available for cylindrical MTF by giving minimum requirements in terms of initial conditions

of the target, and parameters for the heavy-ion beam driver. It is for this reason that our study does neither specify the axial position of the ignition section in an MTF target, nor include artificial axial loss terms that would imply a specific target design. However, we see a broad window in the parameter space of possible MTF designs where axial losses from the ignition section appear to be insignificant.

5. Conclusion

In conclusion, we find that magnetized implosions driven by heavy-ion beams provide a promising means to reach states of high energy density in matter. The beam irradiation geometry is well suited for direct heating of cylindrical targets. Effects of the target magnetization will show up in enhanced peak fuel temperatures and corresponding yields from thermonuclear fusion reactions. In order to prevent the rapid diffusion of magnetic flux during implosions, one has to provide certain minimum values of the initial fuel temperature and of the product $(UR)_0$ of implosion velocity and initial radius, which define the regime of SSMI [4]. An important problem in magnetized implosions is the formation of a boundary layer of cold dense fuel at the fuel-pusher interface of the target. This effect diminishes the neutron yield in magnetized implosions, and might prevent the fuel burn in magnetized fusion targets from propagating radially outwards. We find that the growth rate of the boundary layer mainly depends on the $(UR)_0$ product of the implosion, which is directly related to the driver pulse energy E_b. The SSMI criterion on magnetized implosions can therefore be formulated as a lower limit on $E_b \gtrsim 20$–$40\,\mathrm{kJ\,cm^{-1}}$. Below this limit, the magnetic field and consequently the fuel heat diffuse away before maximum compression has been reached.

As an application of the concept of magnetized implosions, we have investigated ignition conditions for magnetized cylindrical fusion targets. We find that such targets ignite at similar driver energies as compared to spherical ICF targets, but at significantly reduced implosion velocities and fuel ρR values. This means that the conditions on ion driver power and pulse duration are strongly relaxed. The ignition threshold is at roughly $E_b = 10\,\mathrm{MJ}$ per centimetre target length for DT fuel. The large difference to the SSMI energy threshold comes from the fact that, apart from the larger fuel temperatures at ignition, one needs to reach the fuel ρR threshold for magnetized targets, as discussed in more detail in [3]. This requires stronger compression, and therefore larger driver energy. Another marked difference to conventional ICF targets is the large fuel pre-heat of more than 50 eV that is necessary to reach ignition temperatures in cylindrical implosions. Finally, hot-spot ignition, i.e. the propagation of a burn wave along the axis, is found to be essential for high fusion energy gain in cylindrical targets. Without burn propagation, the energy gain of cylindrical targets is very low, namely $G \approx 1$. The process of ignition and the propagation of an axial burn wave in a two-dimensional geometry, as well as specific target designs for cylindrical MTF, have to be investigated in the future.

References

[1] Kirkpatrick R., Lindemuth I. and Ward M. 1995 *Fusion Technol.* **27** 201
[2] Basko M., Kemp A. and Meyer-ter-Vehn J. 2000 *Nucl. Fusion* **40** 59
[3] Kemp A., Basko M. and Meyer-ter-Vehn J. 2001 *Nucl. Fusion* **41** 235
[4] Basko M. 2000 *Phys. Plasmas* **7** 4579
[5] Ramis R., Honrubia J., Ramirez J. and Meyer-ter-Vehn J. 2000 *Inertial Fusion Sciences and Applications—State of the Art 1999* ed C. Labaune, W. Hogan and K. Tanaka (Paris: Elsevier) p 509
[6] Avrorin E. *et al* 1984 *Sov. J. Plasma Phys.* **10** 298
[7] Caruso A. and Strangio C. 1999 *Inertial Fusion Sciences and Applications* ed C. Labaune, W. Hogan and K. Tanaka (Paris: Elsevier) p 88
[8] Ahlen S. 1980 *Rev. Mod. Phys.* **52** 121
[9] Lindl J. 1998 *Inertial Confinement Fusion: The Quest for Ignition and Energy Gain Using Indirect Drive* (New York: Springer)
[10] Braginskii S. 1965 *Rev. Plasma Phys.* **1** 205
[11] Drazin P. and Reid W. 2001 *Hydrodynamic Stability* (Cambridge: Cambridge University Press)
[12] Arnold R. and Meyer-ter-Vehn J. 1988 *Z. Phys.* D **9** 65
[13] Basko M. 1998 *CEA Report* EUR-CEA-FC-1645